Structure

Article

Cooperative mechanics of PR65 scaffold underlies the allosteric regulation of the phosphatase PP2A

Graphical abstract

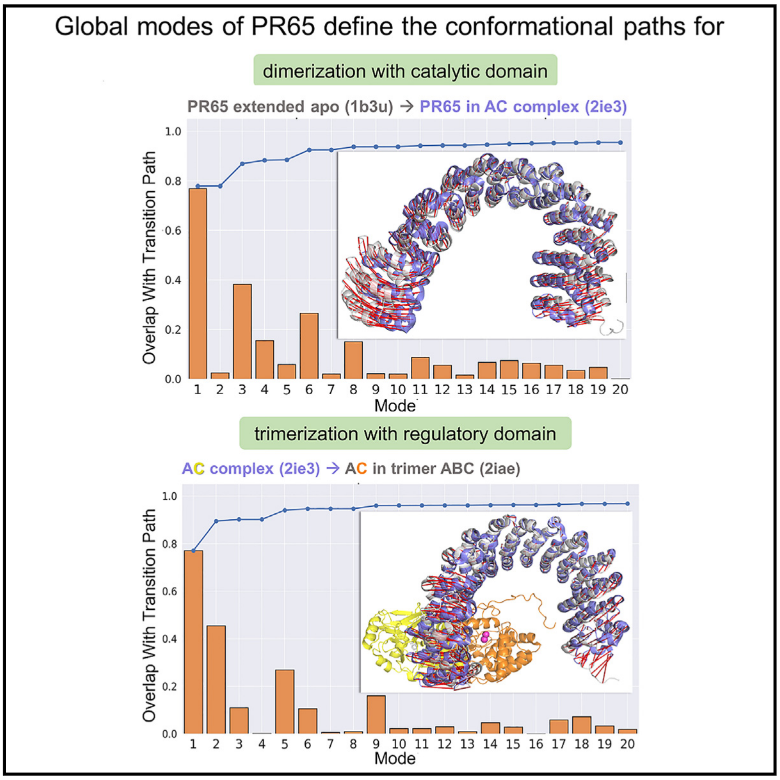

Highlights

- PR65 is a highly elastic scaffold facilitating the allosteric events within PP2A
- PR65 intra-repeat coils stiffen upon participation in the PP2A trimer
- The intrinsic dynamics of PR65 predispose it to binding the catalytic subunit C
- Global modes of the core enzyme AC facilitate its complexation events

Authors

Burak T. Kaynak, Zakaria L. Dahmani, Pemra Doruker, ..., Reuven Gordon, Laura S. Itzhaki, Ivet Bahar

Correspondence

bahar@laufercenter.org

In brief

Kaynak et al. show that the repeat protein PR65 plays a critical role in mediating the catalytic activity and interactions of PP2A, whose dysregulation is implicated in human cancers. The study demonstrates the unique ability of PR65 architecture to adapt to functional changes in conformation and to mechanical stress.

Kaynak et al., 2023, Structure *31*, 607–618
May 4, 2023 © 2023 The Authors. Published by Elsevier Ltd.
https://doi.org/10.1016/j.str.2023.02.012

Structure

CellPress
OPEN ACCESS

Article

Cooperative mechanics of PR65 scaffold underlies the allosteric regulation of the phosphatase PP2A

Burak T. Kaynak,[1,2,7] **Zakaria L. Dahmani,**[1,7] **Pemra Doruker,**[1,7] **Anupam Banerjee,**[1,3] **Shang-Hua Yang,**[4] **Reuven Gordon,**[5] **Laura S. Itzhaki,**[6] **and Ivet Bahar**[3,8,*]
[1]Department of Computational and Systems Biology, School of Medicine, University of Pittsburgh, Pittsburgh, PA 15213, USA
[2]Computational Neurobiology Laboratory, Salk Institute for Biological Studies, La Jolla, CA 92037, USA
[3]Laufer Center for Physical and Quantitative Biology, and Department of Biochemistry and Cell Biology, School of Medicine, Stony Brook University, Stony Brook, NY 11794, USA
[4]Department of Electrical Engineering, National Tsing Hua University, Hsinchu 30013, Taiwan
[5]Department of Electrical and Computer Engineering, University of Victoria, Victoria, BC V8P 5C2, Canada
[6]Department of Pharmacology, University of Cambridge, Tennis Court Road, Cambridge CB2 1PD, UK
[7]These authors contributed equally
[8]Lead contact
*Correspondence: bahar@laufercenter.org
https://doi.org/10.1016/j.str.2023.02.012

SUMMARY

PR65, a horseshoe-shaped scaffold composed of 15 HEAT (observed in Huntingtin, elongation factor 3, protein phosphatase 2A, and the yeast kinase TOR1) repeats, forms, together with catalytic and regulatory subunits, the heterotrimeric protein phosphatase PP2A. We examined the role of PR65 in enabling PP2A enzymatic activity with computations at various levels of complexity, including hybrid approaches that combine full-atomic and elastic network models. Our study points to the high flexibility of this scaffold allowing for end-to-end distance fluctuations of 40–50 Å between compact and extended conformations. Notably, the intrinsic dynamics of PR65 facilitates complexation with the catalytic subunit and is retained in the PP2A complex enabling PR65 to engage the two domains of the catalytic subunit and provide the mechanical framework for enzymatic activity, with support from the regulatory subunit. In particular, the intra-repeat coils at the C-terminal arm play an important role in allosterically mediating the collective dynamics of PP2A, pointing to target sites for modulating PR65 function.

INTRODUCTION

Around one-third of human proteins contain units of varying size and secondary and tertiary structural composition, repeated in tandem.[1] Tandem-repeat proteins such as ankyrin, tetratricopeptide, and HEAT (observed in Huntingtin, elongation factor 3 (EF3), protein phosphatase 2A (PP2A), and the yeast kinase TOR1) repeats have highly versatile three-dimensional shapes arising from the stacking of small secondary-structure motifs of 20–40 amino acids into both quasi-one-dimensional arrays and circular forms.

Repeat proteins have been the subject of intensive study, as their simple architectures make them strikingly amenable to the dissection and redesign of their biophysical properties with potential for exploitation in biotechnology and medicine.[2–6] Helical repeat proteins look like springs and indeed are flexible molecules with spring-like properties.[7–18] Their flexibility is thought to be crucial to their function, although our understanding of how these structures direct functions is limited. Distantly located repeats fold cooperatively, even though the only contacts in these proteins are short-range ones.[19–21] Function may also be transmitted at a distance with allosteric effects, transferred through the repeat array.

Here we explore the conformational mechanics of the HEAT-repeat protein PR65, the elastic "connector" subunit of PP2A. PP2A is a heterotrimeric Ser/Tyr phosphatase that regulates diverse cellular activities.[22] PP2A dysregulation is associated with many types of cancer and other diseases,[23] hence the targeting of PP2A for developing therapeutics.[24] The PR65 scaffold (A) and catalytic (C) subunits form the core of the enzyme. Enzymatic activity is controlled by binding of different regulatory (B) subunits. Figure 1A displays the PP2A holoenzyme[22] where PR65 (Aα isoform; cyan surface) forms a scaffold for recruiting the catalytic (Cα isoform; yellow cartoon) and B56 regulatory (γ1; purple cartoon) subunits on the same side. PR65 in apo state[25] (magenta) undergoes a significant conformational change during complexation (Figure 1B). PR65 consists of 15 HEAT-tandem repeats of two anti-parallel helices each (see

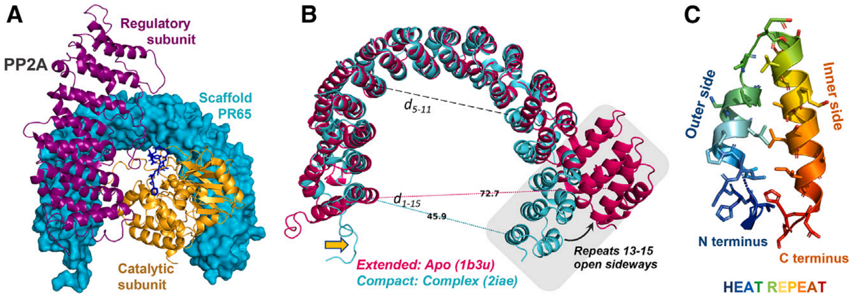

Figure 1. PP2A complex and the PR65 scaffold

(A) PP2A heterotrimer structure and its conformational flexibility. PP2A is composed of three subunits, PR65 (cyan), catalytic (yellow), and regulatory (purple) subunits, and PR65 is composed of 15 HEAT repeats, illustrated in (C). The PDB structure (PDB: 2iae) also contains a peptide (blue sticks) bound to the catalytic subunit.

(B) Extended and compact conformations of the PR65 scaffold. The extended conformation is observed in the apo state of PR65 (PDB: 1b3u). The distance between the C^{α}-atoms of N30 and Y577 (d_{1-15}) indicates an increase of >25 Å (from 45.9 to 72.7 Å) as the repeats 13–15 move out in the extended structure relative to their position observed in PP2A complex. In contrast, the distance between inner repeats 5 and 11 (black dashed line, d_{5-11}) does not change significantly.

(C) The HEAT motif: The N-terminal helix lines the inner surface of the PR65 horseshoe-like scaffold, and the C-terminal helix lies at the outer surface. A network of hydrophobic contacts stabilizes the motif.

Figure 1C). Here, the B56γ1 subunit is composed of eight pseudo-HEAT repeats.

In previous work by Grinthal et al.,[11] 2-ns molecular dynamics (MD) simulations were performed by applying a constant uniaxial tension or compression at the two ends of PR65. In the low-force regime, application of a series of fixed forces up to 150 pN during tension experiments (or $\leq$70 pN during compression) led to gradual extension (or contraction) of the scaffold until it reached an equilibrium end-to-end distance dependent on the exerted force, and to it returning almost reversibly to its original state upon release of the force. At higher forces, on the other hand, the system could not recover its original shape, indicating that there were irreversible changes, e.g., disruptions at specific helix-helix interfaces or fractures at interhelix turns, which underlie the viscoelastic behavior of PR65.

In the first part of our study, we elucidate the intrinsic dynamics of PR65 and its complexes in solution (closer to *in vivo* conditions) without the application of any external forces. We performed simulations at various levels of complexity, including MD, elastic network model (ENM) analyses,[26] and a hybrid approach (ClustENMD)[27,28] for conformational sampling. We demonstrated that the apo PR65 scaffold is extremely flexible with its arms opening/closing by 30–40Å multiple times during 200-ns runs. This intrinsic elasticity is also evident and consistent with the global modes of motion (the lowest-frequency modes, also called soft modes) deduced from either ENM-based or full-atomic normal mode analyses (NMAs). We obtained a clear picture on the broadening of mode frequencies due the conformational variability of PR65 by performing ENM analyses on multiple MD snapshots. Our hybrid simulations elucidate how complexation with the catalytic and regulatory subunits alters the conformational dynamics of the scaffold. We further demonstrated that the global modes intrinsically accessible to PR65, predicted by ENM, facilitate the PR65 conformational changes occurring upon formation of the core enzyme (AC complex), and those accessible to AC favor its conformation selected in the PP2A trimer.

In the second part, we characterize the response of PR65 to stress toward understanding its mechanical behavior in the apo form and in the PP2A complex using our ENM-based tool MechStiff.[29] We identified the critical sites that endow those mechanical properties, and we point to the correlation between residue-based stiffness profile and evolutionary conservation across the scaffold. These findings underline the functional importance of the mechanical properties of the PR65 scaffold, and they reveal the critical sites that can be subjected to ligand binding for customized modulation of function.

RESULTS

Large fluctuations in PR65 end-to-end distance mainly result from the reconfiguration of the HEAT repeats 1–4 and 12–15

The end-to-end distance of the PR65 scaffold is a natural metric for analyzing its conformational dynamics and flexibility. However, the N-terminal helix, belonging to the first HEAT-repeat unit, is unfolded in the PP2A complex considered in the present study, as indicated by the yellow arrow in Figure 1B. To avoid the variability resulting from this unstructured region, we monitored the distance (d_{1-15}) between the C^{α}-atoms of N30 and Y577, on the inward-facing helices of repeats 1 and 15, respectively. The PR65 arms extend more than 25 Å away as the scaffold reconfigures from compact (chain A in PP2A, d_{1-15} = 45.9 Å) to extended (apo, d_{1-15} = 72.7 Å) state, as shown in Figure 1B.

Figure 2A displays the time evolution of this distance d_{1-15} during the four MD simulations, initiated from compact (*C1* and *C2*) and extended (*E1* and *E2*) conformers. Notably, the scaffold fluctuates between the compact and extended states multiple times during these runs (of 200 ns each). The median for d_{1-15} is 67.4 Å in *C1*, 54.9 Å in *C2*, 79.6 Å in *E1*, and 75.9 Å in *E2*, indicating that extended conformers are sampled more readily in all runs presumably due to an entropic effect in favor of the extended form. The d_{1-15} distance can occasionally exceed 90 Å, which is appreciably larger than that observed in the apo crystal structure (72.7 Å).

The second distance plotted in Figure 2A is d_{5-11} between the inward-facing helices on the respective repeats 5 and 11, specifically between M180 and R418 C^{α} atoms. In contrast to d_{1-15}, d_{5-11} fluctuates within a narrow band, consistent with the original d_{5-11} of 44.7 Å and 48.4 Å by the compact and extended crystal structures, respectively. Thus, the central repeats between 5 and 11 tend to preserve their original curvature in all runs (see also Figure 1B). The overall picture that emerges from our MD simulations is that the central part of the scaffold (repeats 5–11)

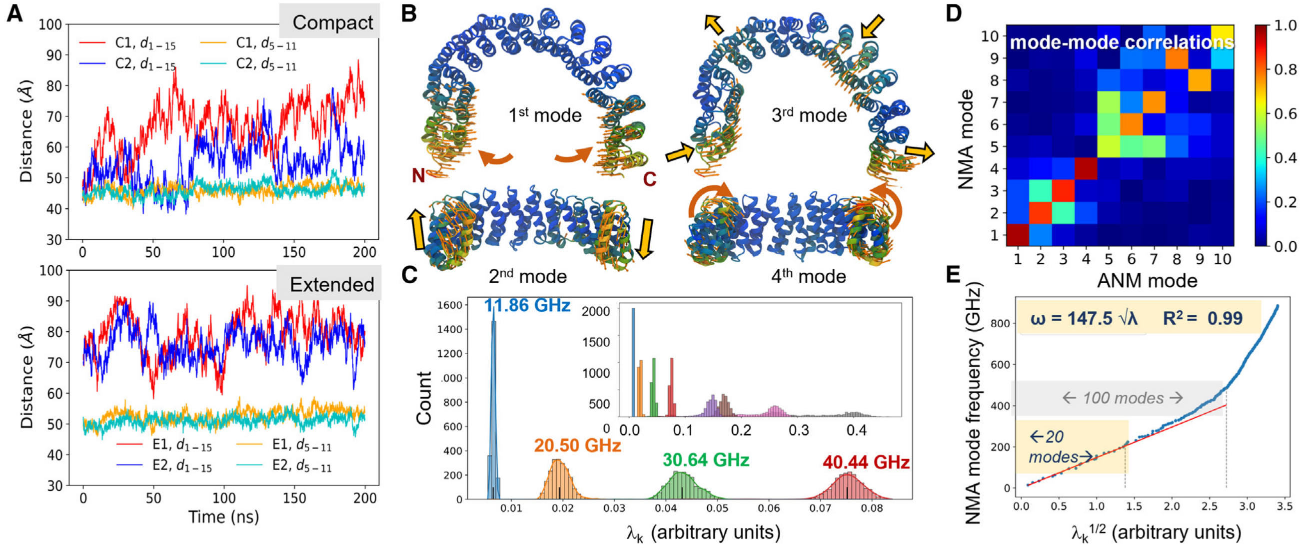

Figure 2. Dynamics of PR65

(A) Fluctuations in PR65 inter-repeat distances, d_{1-15} and d_{5-11}, during MD simulations. The top panel refers to the runs *C1* and *C2* with the compact conformer of PR65 used as input (see the distances around 45 Å at t = 0), and the bottom panel to those, *E1* and *E2*, conducted using the extended conformer. d_{1-15} shows large fluctuations in both cases. The compact form approaches the extended form within the timescale (200 ns) of simulations, whereas the extended form fluctuates in the range 60–90 Å. The inner distance d_{5-11} exhibits minimal fluctuations in both cases.

(B) Global modes of motion predicted by the ANM. The slowest four modes are shown for the compact conformer by color-coded ribbon diagrams. Blue regions exhibit minimal displacements; yellow-green regions undergo large displacements along the directions indicated by the arrows.

(C) Distribution of ANM eigenvalues based on 2,000 snapshots from MD run *C2*. Mode frequencies are spread/broadened due to the conformational fluctuations. The first four modes' frequencies display well-separated Gaussian distributions. In contrast, the higher modes (see inset showing modes 1-8) display broader and partially overlapping distributions. Black vertical bars at the center of the histograms represent the corresponding medians. The labeled frequencies are obtained after rescaling ANM frequencies with respect to those from full-atomic NMA in (E).

(D) Overlap matrix (correlation cosines) between the first 10 modes from atomic NMA and those from ANM.

(E) NMA vs, ANM frequencies of the first 300 modes for compact PR65. Red line is fitted to the first 20 modes with $R^2 > 0.99$. See the counterpart of (E) for all four conformers in Figure S2A.

closely maintains its overall conformation, while the outer four repeats on both sides (repeats 1–4 and 12–15) are highly flexible and their cooperative reconfigurations underlie the opening and closing of the scaffold.

The ability of PR65 to undergo large end-to-end distance fluctuations is endowed by its global modes of motion uniquely defined by its tandem-repeat architecture

Previous studies have repeatedly shown the significance of low-frequency modes, also called global modes, predicted by anisotropic network model (ANM), in supporting biological function.[30,31] Figure 2B illustrates the first four global modes predicted for PR65 using its compact conformer in PP2A (PDB: 2iae),[22] and Video S1 displays the first three modes of the compact and extended forms of PR65. The diagrams are color coded by the displacements of the residues, from blue (most rigid) to yellow (most flexible), and the vectors indicate the direction and size of displacements for relatively mobile residues. The three repeats at the N and C termini constitute the most mobile regions of the horseshoe, as clearly observed in the first mode. The high mobility of the arms and the restrictions on the central part of PR65 are consistent with the large changes in d_{1-15} and the relatively limited fluctuations in d_{5-11} observed in MD runs.

Each of the first four modes illustrated in Figure 2B describes a cooperative mechanism of motion: in-plane stretching/compression that induces an overall extension/contraction (mode 1), opposite direction out-of-plane up and down movements of the arms accompanied by slight rotations (mode 2) as best viewed from the side, smaller amplitude in-plane undulating/twisting motions of subsets of repeats (mode 3), and concerted rolling of the ends (mode 4). Previously, Grinthal et al.[11] performed classical NMA on the extended, apo conformer of PR65 (PDB: 1b3u).[25] They defined the first two modes as "uniform, in-plane increase and decrease in the overall curvature" and "overall twisting motion distributed uniformly along the length of the structure," respectively, consistent with the present predictions based on the compact form. Corresponding mode frequencies were reported as 11.1 and 24.3 GHz. They also showed that these two modes cumulatively accounted for a large extent of the conformational changes between the extended and compact conformers. The contributions of the individual ANM modes ($1 \le k \le 10$) to the overall dynamics computed here are presented in Figure S1. The bar plot shows that the first mode accounts for 34% of the PR65 dynamics in the compact form and 38% in the extended form, and the second mode 13.2% and 10.3%, respectively, and the cumulative contribution of the first three modes is above 50% in both forms.

Our analysis therefore shows that the ability of PR65 to undergo large (~30Å) distance fluctuations between its ends is encoded in its architecture that favors (as the softest or lowest-frequency modes) such coupled opening/closing of the two ends, and especially three to four repeat units at both ends. These regions are distinguished by their high mobility in global modes 1–4, which assist in the cooperative rearrangements that are apparently used for stabilizing the trimeric phosphatase. Thus, the global movements are not uniformly distributed over all repeats but affect the terminal repeats more strongly than the inner ones.

MD snapshots combined with ANM analysis permit us to evaluate the broadening of the dispersion of collective modes' frequencies

We performed classical NMA, using as input snapshots selected from the MD runs *C1*, *C2*, *E1*, and *E2*. Table S1 lists the frequencies of the first four normal modes computed for each case. The frequencies of the extended conformers are higher than those of the compact conformers in general, indicating that the structure is more strained/relaxed in the extended/compact form. Given that the mode frequencies may be sensitive to variations in conformations, which presumably underlie the broadening effect in experimentally observed histograms of vibrational frequencies, we performed an ANM analysis for a large ensemble of conformers sampled during the four MD simulations. Such an extensive analysis is supported by the computational efficiency of ANM, as ANM analysis does not require any energy minimization prior to spectral decomposition and yields a unique analytical solution for each conformer. Figure 2C overlays the resulting histograms for the global modes sampled in run *C2*. Even though this run starts from the compact conformer, it also visits the extended state several times during 200 ns (blue curve in Figure 2A upper panel). Thus, the conformational variability of the scaffold results in the broadening of the ANM frequencies. This broadening effect becomes more pronounced as the mode index increases. While the distributions for the first four modes are well separated, distributions of those of the higher modes are not. The increasingly higher overlaps between the frequency ranges of modes 5–8 can be seen in the inset.

PR65 cooperative mechanisms of motions and their frequency dispersion captured by ENMs show agreement with those inferred from full-atomic NMA

Next, we examined to what extent the shapes of the ANM global modes were similar to those obtained by classical NMA. These mode-mode similarities were assessed by generating the correlation cosines between the top 10 modes, presented in Figure 2D for the compact conformer. The first four modes are robustly maintained (correlation cosine >0.90) and modes 6–10 exhibit high correlation (while the orders of modes 8 and 9 are swapped). ANM mode 5 shows a moderate correlation with its NMA counterpart; however, its correlation cosine (of 0.6 with NMA mode 5) is significantly enhanced by the contributions of NMA modes 6–7, suggesting that this normal mode is represented by the partial contribution of these three modes. This analysis consistently reveals that the same global modes are reproduced, irrespective of the resolution of the spectral analysis.

As a further analysis, we examined the frequencies of global modes obtained by ANM and classical NMA. Figure 2E displays the comparison for the top-ranking 300 modes (each represented by a dot). It is important to note that the higher resolution (and the use of full-fledge force field) of atomic NMA does not affect the low-frequency end of the mode spectrum, e.g., the top-ranking 20 modes, which, in principle, refers to collective movements of substructures being insensitive to atomic details and precise interactions. This permits us to deduce from the fixed slope of this plot in this regime the proportionality constant to evaluate the ANM frequencies (proportional to $\lambda_k^{1/2}$ for mode *k*) in gigahertz. The inset shows this linear relationship, which yields a value of γ = 0.31 kcal/(mol. Å^2) = 0.22 N/m for the ANM inter-residue spring constant, using Equation 4 in STAR Methods. The median frequencies written in Figure 2C for modes 1–4 are obtained using this force constant in the ANM.

Note that γ is a *local* property dependent on the tightness of associations between residue pairs in the folded protein, and, as such, it is expected to show little dependence on the *global* conformation, hence the minimal differences in the slopes of the curves for compact and extended conformers as illustrated in Figure S2A. In fact, rescaling of γ based on the NMA frequencies obtained for the conformers *C1*, *C2*, *E1*, and *E2* yields the value of γ = 0.312 ± 0.019 kcal/(mol. Å^2) for PR65 (see Figure S2A and supplemental information). The value of γ is often predicted by comparison with experimental B-factors using Equation 3. If we use the experimental data for extended apo structure of PR65, we obtain γ = 0.915 kcal/(mol.Å^2), whereas using 14 experimentally measured B-factors extracted from the PDB files including complexes yields γ = 0.456 ± 0.139 kcal/(mol.Å^2).

While the force constant is a material property independent of the overall conformation, the frequencies of the global modes (i.e., eigenvalues of the ANM Hessian) as well as the mode shapes (eigenvectors) depend on the overall conformation. Figures S2B–S2E display the frequencies of ANM global modes ($1 \leq k \leq 20$) for the two extended and two compact conformers, showing (1) the close reproducibility of the results between the two extended forms (in accord with full-atomic NMA), as well as that between the two compact forms; and (2) the differences between the operating frequencies in the extended and compact forms (see also Table S1), the frequencies of the extended (more strained) conformers being higher in general. Likewise, the mode-mode overlap heatmap in Figure S3A shows that the shapes of the modes accessible to the two forms gradually differentiate as higher modes are considered, whereas the lowest-frequency three modes are robustly shared between the two forms (see also Video S1). Overall, this analysis confirms the robustness of global modes of motion intrinsically accessible to the PR65 scaffold, the functional significance of which will be clear in the context of the dynamics of PP2A.

Binding of the catalytic subunit reinstates the regular dynamics of C-terminal HEAT repeats of PR65, whereas binding of the regulatory subunit enhances the cooperativity across PR65

To compare the global dynamics of PR65 in its isolated unbound form and in complex with regulatory subunit B and catalytic subunit C, we performed ClustENMD runs for PP2A heterotrimer (PDB: 2iae, chains A, B, and C), isolated PR65 (chain A), and the dimer of PR65 and the catalytic subunit (chains A and C, extracted from trimer). These hybrid simulations are highly efficient; e.g., ClustENMD run takes 20 min compared with 8 days for a 100-ns MD simulation of PR65. The conformational space predicted by

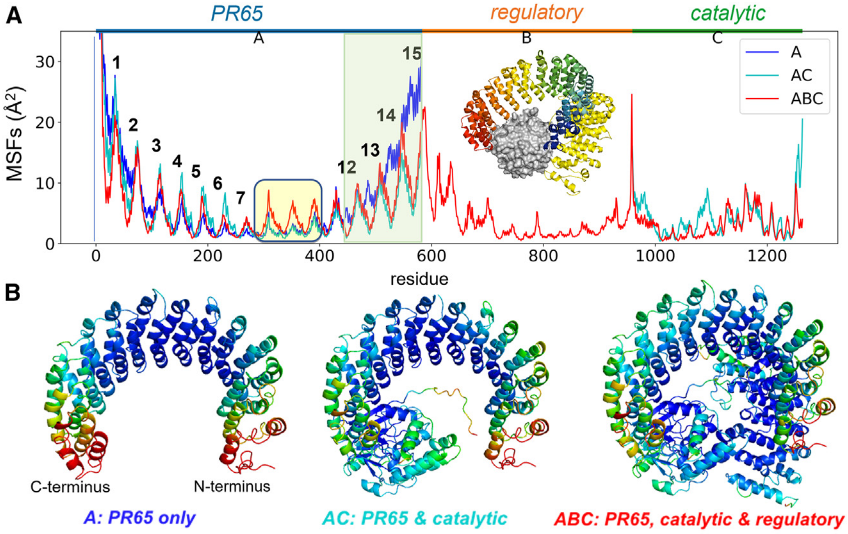

Figure 3. Comparison of residue mobilities in PR65 and its complexes based on ClustENMD simulations

(A) The residue MSFs in the runs performed for unbound PR65 (blue curve), the dimer AC (PR65 and catalytic C subunit; cyan), and the heterotrimer ABC (red). HEAT-repeat numbers are indicated for some of the repeats in PR65.

(B) Each structure is color-coded based on MSFs. Binding of the regulatory subunit (chain B in ABC complex) increases the fluctuations in the middle of the PR65 scaffold (yellow box in the top panel), while repeats 12–15 get ordered upon binding the catalytic subunit (see the light-green box).

ClustENMD shows a high correlation with experiments (for molecular systems resolved in multiple conformational states).[32]

The mean-square fluctuation (MSF) profiles of amino acids of the three systems (referred to as A, AC, and ABC) are plotted in Figure 3A based on 600 conformers generated by ClustENMD for each system. In all cases, the mobility increases toward the ends of the PR65 scaffold. The oscillatory behavior of PR65 reflects the 15-HEAT-repeat architecture of PR65: peaks occur at the inter-repeat loops, and minima at the intra-repeat turns and C-terminal helices of the helix-turn-helix repeats, which face the horseshoe interior. The fluctuations at the N terminus are highly consistent with the unwinding of the terminal helix. The high fluctuations at the C-terminal arm, on the other hand, originate from an inherent conformational variability intrinsic to repeats 12–15. The fluctuation behavior of these repeats (highlighted in the semi-transparent green box) is distinguished from all others as the regular pattern of minima and maxima is disrupted. Notably, binding of the catalytic subunit near repeats 12–15 (see Figure 1A) restores the regular pattern, as the comparison of the blue (A) and cyan (AC complex) curves reveals (PR65 makes close contacts with the catalytic subunit at repeat 12). This regular pattern persists in the trimer also (ABC, red curve), where the binding of the regulatory subunit (B) does not alter the dynamics of the C-terminal arm but induces an increased mobility at the central part of the scaffold (enclosed in the yellow box in the figure), especially at the outer helices of repeats 9 and 10, and overall strengthens the communication (that propagates via fluctuations) across neighboring repeats. The bottom panel shows the ribbon diagrams for the three cases, color coded by residue MSFs. The diagrams clearly show the most mobile regions (red) and the higher mobility of the outer helices of the repeats compared with their inner helices.

The regulatory subunit of PP2A allosterically couples the PR65 C- and N-terminal arms to the catalytic subunit domains *1* and *2* to support enzymatic mechanics

Results from further analysis of PR65 global dynamics in the isolated form (A), in the complex with the catalytic subunit (AC), and in the trimeric PP2A are presented in Figure 4. Heat maps in Figures 4A–4C show the orientational cross-correlation between residue motions, computed for the PR65 alone, PR65 in the dimer with the catalytic subunit, and PR65 in the trimer, respectively. Figures 4D and 4E display the cross-correlations for the entire dimer and trimer, respectively. The black lines separate the individual subunits, and the chain identifiers and residue numbers are provided along the abscissa and ordinate.

In the isolated PR65 (Figure 4A), there are two equally sized (red) blocks at the N and C termini, both corresponding to four repeat units. These positively correlated blocks along the diagonal reflect the concerted internal movements of the subsets of four repeat units at each end, and the off-diagonal blue blocks show that the two subsets correlate but fluctuate in opposite directions (they are anticorrelated). The anticorrelated movements are consistent with the stretching/contraction observed in mode 1 in Figure 2B, indicating the dominant effect of mode 1. The middle part presents a narrower band of positive correlations compared with the two terminal blocks of four repeats.

Comparison of Figures 4A and 4B shows that the repetitive pattern of the repeat units, especially that of C-terminal units, becomes more pronounced upon binding the catalytic subunit. We also note that PR65 in this dimeric form (AC) exhibits anticorrelated movements between consecutive blocks of three to four repeats. These observations are consistent with the coupled movements predicted in in mode 3 (Figure 2B). In the heterotrimer (Figure 2C), there is an overall strengthening in the cooperativity of the adjacent HEAT repeats across the scaffold (shown by the widened red band along the diagonal). This may facilitate the allosteric signal transduction across the scaffold. The concerted motions of the N-terminal repeats 1–4 propagate to the near neighbors in the N-terminal half of PR65, up to repeat 10, while the C-terminal repeats 12–15 are distinguished by accentuated anticorrelated (blue) movements with respect to the rest of the scaffold. Thus, binding of the regulatory subunit significantly affects the cross-correlations between the residues of the scaffold, increasing the overall correlations along the scaffold and engaging the central repeats to coherently propagate signals, as also hinted by Figure 5A.

Notably, in the dimeric complex (Figure 4D), the catalytic subunit is divided into two internally correlated domains, *dom1* and *dom2*, illustrated in Figure 4F; *dom1* binds to the C-terminal arm of PR65 and its movements are correlated with those of the

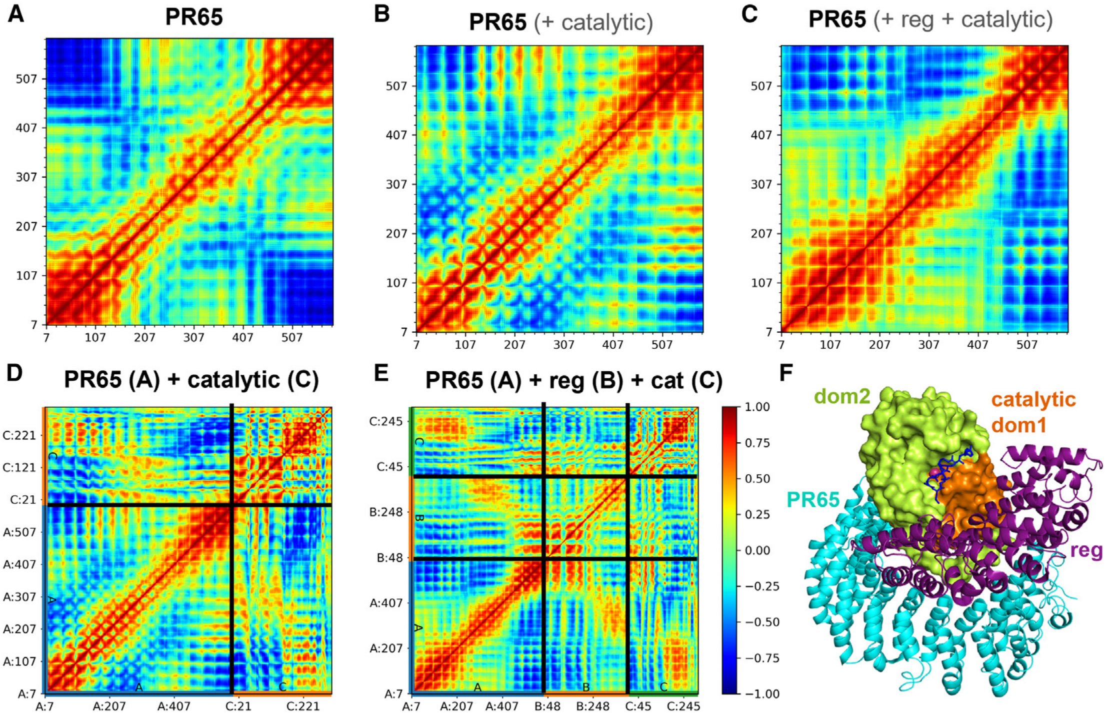

Figure 4. Residue cross-correlations based on ClustENMD conformers

(A–C) Cross-correlation maps for PR65 along (A), PR65 in the dimer AC (B), and PR65 in ABC (C).

(D and E) The cross-correlations for AC (D) and ABC (E). Subunits are separated by black lines. Cross-correlations are based on all conformers/simulations also reported in Figure 3.

(F) The two domains (orange and lime, surface representation) of the catalytic subunit bound to the PR65 scaffold (cyan) and regulatory subunit (purple). A peptide (blue sticks) and metal ions (red sphere) are located at the catalytic cleft between the two domains.

C-terminal arm and anticorrelated with the N-terminal arm. Upon binding of the regulatory subunit (Figure 4E), the anticorrelated movements of the N-terminal arm with respect to *dom1* spread to a larger portion (up to repeat 10) of the scaffold. Thus, a strong cooperativity is induced, which encompasses repeats 1–10, and the N-terminal arm moves in concert with *dom2* of the catalytic subunit even though it does not make direct contacts. The regulatory subunit thus serves as an allosteric agent strengthening the cooperativity of almost the entire scaffold, with repeat unit 11 acting as a hinge site. Notably, *dom1* continues to be coupled to the C-terminal arm with which it makes direct contacts.

Overall, this analysis highlights the importance of the regulatory subunit for inducing a high cooperativity across HEAT repeats 1–10 of PR65, accentuating the anticorrelated movements of C-terminal repeats 12–15 with respect to the rest of the scaffold, and enhancing the correlated movements of the C-terminal repeats with *dom1* and the N-terminal repeats with *dom2*. This type of allosteric coupling of both ends of PR65 to the two domains of the catalytic subunit, mediated by the regulatory subunit, may be essential to facilitating the opening/closing of the catalytic cleft in tandem with the stretching/contraction of PR65 in its intrinsically accessible (global) mode 1.

Further investigation of the collective dynamics of PP2A verified that the global stretching/contraction mode of PR65 is retained as the softest mode of the trimer (see Figure S3B). Notably, the same mode operates almost invariably in both the compact and extended forms of PR65, indeed providing a path for the passage between these two forms (Figure S3A). Furthermore, Figure S3B shows that the first five modes intrinsically accessible to PR65 are operational in the trimer (the fourth being represented by a combination of a few slow modes of the trimer). In particular, the global modes 2 and 5 closely retain their identity in the trimer (with a correlation cosine >0.77). Note that, in the 3N-dimensional space of modes, this is an enrichment of several orders of magnitude compared with the random correlation cosine of $(3N)^{-1/2}$, where N is the number of residues/nodes in the ANM.

Video S2 illustrates the first (lowest-frequency) mode accessible to the trimer, where the scaffold retains its intrinsically accessible stretching/contraction (mode 1 in Figure 2B) now engaging the catalytic subunit, supported by the regulatory subunit.

Global modes enable the conformational transition of PR65 to form the core enzyme AC, and that of AC to bind the regulatory subunit B to form the full ABC complex

As the flexible scaffold undergoes complexation with different partners, we examined whether the global modes facilitate its conformational transitions. First, we investigated the transition of the apo PR65 (1b3u) upon binding the catalytic subunit to form the so-called core enzyme or the AC complex (Figure 5A). The root-mean-square deviation (RMSD) undergone by PR65 is 2.7 Å during this transition. We concentrated on the deformation vector between PR65 conformation in the extended apo

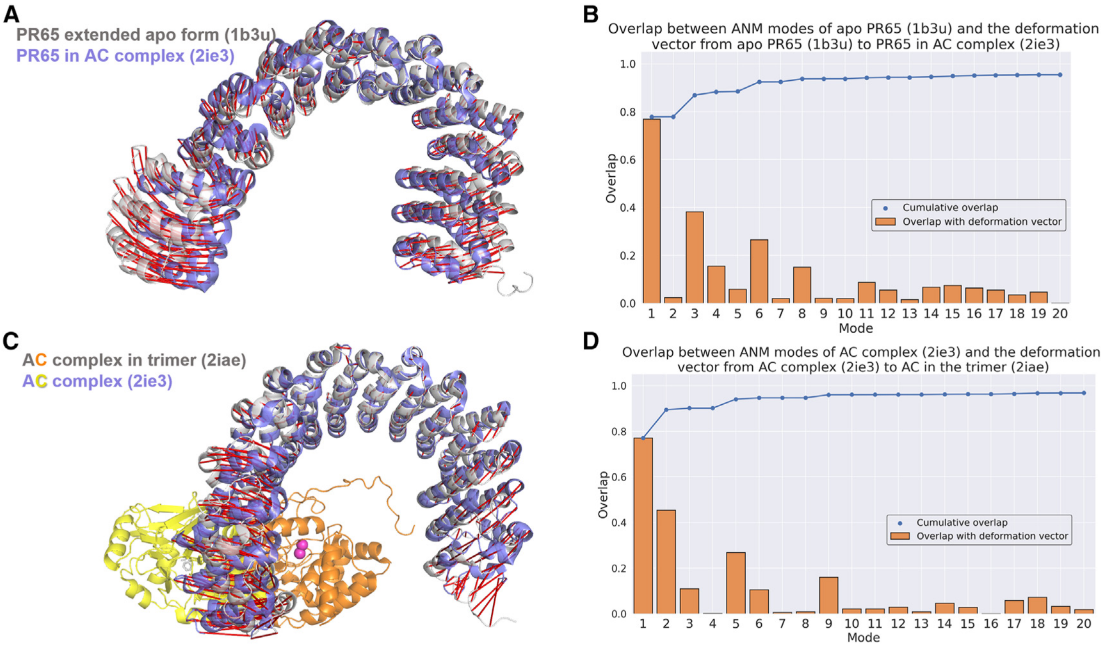

Figure 5. The conformational transitions of the scaffold A and of the core enzyme AC are enabled by the global modes of motion

(A) Superposition of A in the extended apo PR65 (gray; PDB: 1b3u) and PR65 in the complex AC (blue; PDB: 2ie3). Red lines indicate the deformation vector between the two conformers.

(B) The overlap (correlation cosine) between the first 20 ANM modes of apo PR65 with the deformation vector in (A).

(C and D) Same as (A) and (B), for the deformation of AC from the core enzyme (PR65 in blue and catalytic subunit C in yellow; PDB: 2ie3) to AC in the PP2A trimer (PR65 in gray and catalytic subunit C in orange; PDB: 2iae). The cumulative overlap in (B) and (D) is shown by the blue line with dots.

structure and that in the crystal structure of the AC complex (PDB: 2ie3),[33] which is shown by the red lines connecting the same residues on both structures. Our aim is to gauge the propensity of PR65 collective motions for driving it toward the specific conformation in the AC complex. Figure 5B displays the correlation cosine (overlap) between this deformation vector and each global ANM mode. The first mode with a remarkably high overlap value of 0.77 effectively drives the transition between the PR65 conformers in the apo form and in the AC complex. The cumulative overlap of first three modes is 0.89, which collectively account for more than half of the total variance (see Figure S4).

Next, we concentrate on the transitions undergone by the core enzyme (AC complex, PDB: 2ie3). In the crystal structure of this dimeric complex bound to an inhibitor, the position of the catalytic subunit is quite different from that in the ABC complex (Figure 5C). The RMSD is 6.7 Å for this AC transition between the core enzyme and its counterpart in the ABC trimer (PDB: 2iae). We examined whether the global modes of AC enable the conformational transition taking place during complexation with the regulatory B subunit B56. The first mode shows a strong correlation (overlap > 0.75) with the deformation vector (Figure 5D), and the cumulative overlap of the first two modes is above 0.9. The first mode of AC is in fact a twisting motion, rather than a stretching contraction, as illustrated in Video S3 (A in blue and C in yellow). It is evident that the twisting motion repositions the AC dimer for complexation with the regulatory subunit in PP2A (A in gray and C in orange).

Another interesting complexation event for the core enzyme has been observed in a dual-enzyme complex, namely the Integrator-PP2A complex (INTAC) (PDB:7cun).[34] The 12-mer INTAC is a platform that combines an RNA endonuclease with the dephosphorylation activity provided by the PP2A core enzyme. Interestingly, the positioning of the catalytic subunit is similar to that found in PP2A (ABC complex). In Figure S5, we present the high correlations of the first and second modes of the AC core with this conformational transition experienced upon complexation with the integrator INTAC.

Mechanical resistance of PR65 to uniaxial deformation depends on the application site of the force and is enhanced in the trimeric complex

Next, we present a detailed analysis of the effect of complexation and conformational state on the mechanical response of PR65 to uniaxial tension/compression as examined in atomic force microscopy (AFM) or optical tweezer experiments. Using the *MechStiff* module[29] of *ProDy*,[35] we analyzed the following systems: (1) intact PP2A holoenzyme (PDB: 2iae, trimer ABC), in compact form; (2) compact PR65 conformer extracted from this trimer; and (3) extended PR65 conformer resolved in apo state (PDB: 1b3u, chain A). Comparative analysis of systems (1) and (2) reveals the effect of complexation on the mechanical properties of PR65; whereas (2) and (3) provide information on the effect of the PR65 conformational change (extended to compact).

The heatmap in Figure 6A displays the mechanical resistance map for PP2A, where the color-coded ij^{th} entry represents the effective force constant, also called resistance or stiffness, $<\kappa_{ij}>$, of the overall molecule in response to a uniaxial deformation applied to residues *i* and *j* (see the color-coded bar on the right). The catalytic subunit is distinguished by high resistance to deformation, (see the abundance of green to blue entries at the upper right block of the map). In contrast, PR65 exhibits strong resistance around the main diagonal only (enclosed in ellipse); i.e., sequentially close pairs exhibit a high resistance to deformation. This reflects the smaller number of ways (or degrees of freedom) sequentially close pairs can accommodate the deformation due to restrictions imposed by connectivity and bonded interactions. The regulatory subunit (middle box) exhibits an intermediate behavior.

Figures 6B and 6C display the residue-averaged resistances, $<\kappa_i> = \Sigma_j \kappa_{ij}/N$. These usually lie in the range 3–5.5 kcal/(mol.Å^2), with the stiffest residues belonging to the catalytic subunit and the softest at PR65 N terminus. The stiffness of the catalytic subunit originates from its overall tightest packing, consistent with the requirement of high stability and precision near the catalytic site to enable the specific chemical reaction. The color-coded diagram in Figure 6D shows that the inter-repeat loops are more flexible (gray/white) than intra-repeat loops (blue), and that inner residues in the horseshoe-like architecture are stiffer than others. Figure S6A provides additional color-coded diagrams shown from different perspectives.

Further examination of PR65 (alone) compared with its behavior in the trimer showed that trimerization induces an increase in the resistance to tension exerted at spatially (and sequentially) distant pairs, as can be seen in Figure S6B. Therein the two boxes show that the "yielding pairs" are more populated in the isolated PR65 compared with the trimer; i.e., trimerization spatially restricts the PR65 N and C arms, consistent with the coupling of the C-terminal repeats to the catalytic subunit, and N-terminal repeats to the regulatory subunit during the PP2A collective dynamics, as presented above.

Complexation significantly stiffens the intra-repeat loops of PR65 while having minimal effect on the inter-repeat loops

Next, we compared the profiles of PR65 scaffold within the complex (compact in trimer) with its isolated counterpart extracted from the complex (compact conformer; PDB: 2iae, only chain A) and the apo form (extended conformer; PDB: 1b3u). The profiles in Figure 6E show that the mechanical behavior of PR65 in isolation is retained with minimal change (correlation coefficient of 0.92) between the extended and compact forms. Note that this reflects the intrinsic response of this architecture to uniaxial deformation, tension, or compression; i.e., one or the other form is not necessarily more "stressed" in this type of evaluation. In the trimeric complex, on the other hand, the resistance of PR65 is enhanced due to coupling to catalytic and regulatory subunits. For better visualization, we listed along the upper abscissa the positions of the repeat units and indicated the central part of each intra-repeat loop with a dashed vertical line. As expected, these loops (as well as the inter-repeat loops) show sharp minima consistent with their conformational malleability. The lower plot shows the change in stiffening induced upon trimerization. Strikingly, intra-repeat loop regions are distinguished by their maximal stiffening (peaks). We note that complexation induces significant stiffening at the C-terminal repeats' intra-repeat loops. These regions directly interact with the catalytic subunit. The increase in $<\kappa_i>$ is indicative of the induction of a stronger cooperativity across the scaffold in the trimer. The N-terminal repeats also experience a stiffening upon complexation, presumably due to their interaction with the regulatory subunit (see Figure S6).

Overall, while the mechanical character of the PR65 scaffold is maintained (as shown by the correlation coefficient of $R = 0.85$ between the compact PR65 in isolation and that in the trimer, and even $R = 0.73$ with the extended PR65 in isolation and the compact form in the trimer), the complexation with the catalytic and regulatory subunits endows PR65 with strong allosteric properties, and this effect is most pronounced at the N- and C-terminal repeats 3 and 13–15 respectively. Repeat 12 exhibits a peculiar behavior, where there is a softening rather than stiffening upon trimerization at its first helix. This region (containing inter-repeat residues G432–G436) emerges as a potential site for modulating the overall mechanics of the phosphatase, e.g., by small molecule ligand binding, due to its local flexibility as well as interfacial/hinge position between the relatively rigid central part of the scaffold and the relatively flexible C-terminal arm composed of repeats 13–15.

The intrinsic mechanical properties of PR65 are evolutionarily conserved

Previous work has pointed to the significance of mechanical properties for enabling biological function, the regions distinguished by important mechanical roles also being evolutionarily conserved.[36,37] Figure 7C and 7D depict PR65 compact structure color coded by the conservation score of amino acids, evaluated by ConSurf.[38,39] Interestingly, the conservation pattern is generally in accord with the stiffness pattern depicted in Figures 6D and S6A, as well as its further differentiation upon complexation (Figures 7A and 7B), including the different characters of the top and bottom parts of the scaffold. Residues facing the top part (when the N terminus is placed on the left; Figures 7A and 7C) are evolutionarily more conserved. These correspond to the intra-repeat loops. In contrast, residues in the bottom corresponding to inter-repeat loops are less conserved. The regulatory and catalytic subunits both bind to the conserved side of the horseshoe, which harbors the intra-repeat coils (see Figure S7).

DISCUSSION

The structures of repeat proteins underline their spring-like characteristics. Strikingly, in the case of PR65, the multiple snapshots provided by the protein both in uncomplexed and in different complexed forms hint at just how flexible a molecule it is. Notably, this high flexibility is also accompanied by a robust mechanical behavior and stiffening upon participation in the trimeric PP2A. Our findings highlight the unique mechanical properties of the PR65 scaffold endowed by its tandem-repeat architecture and how the structure-encoded intrinsic dynamics of this subunit, complemented by the regulatory subunit, provides a framework for establishing allosteric communication and assisting in the catalytic activity of PP2A. The high mobility of repeats 12–15 may be a prerequisite for facilitating the binding

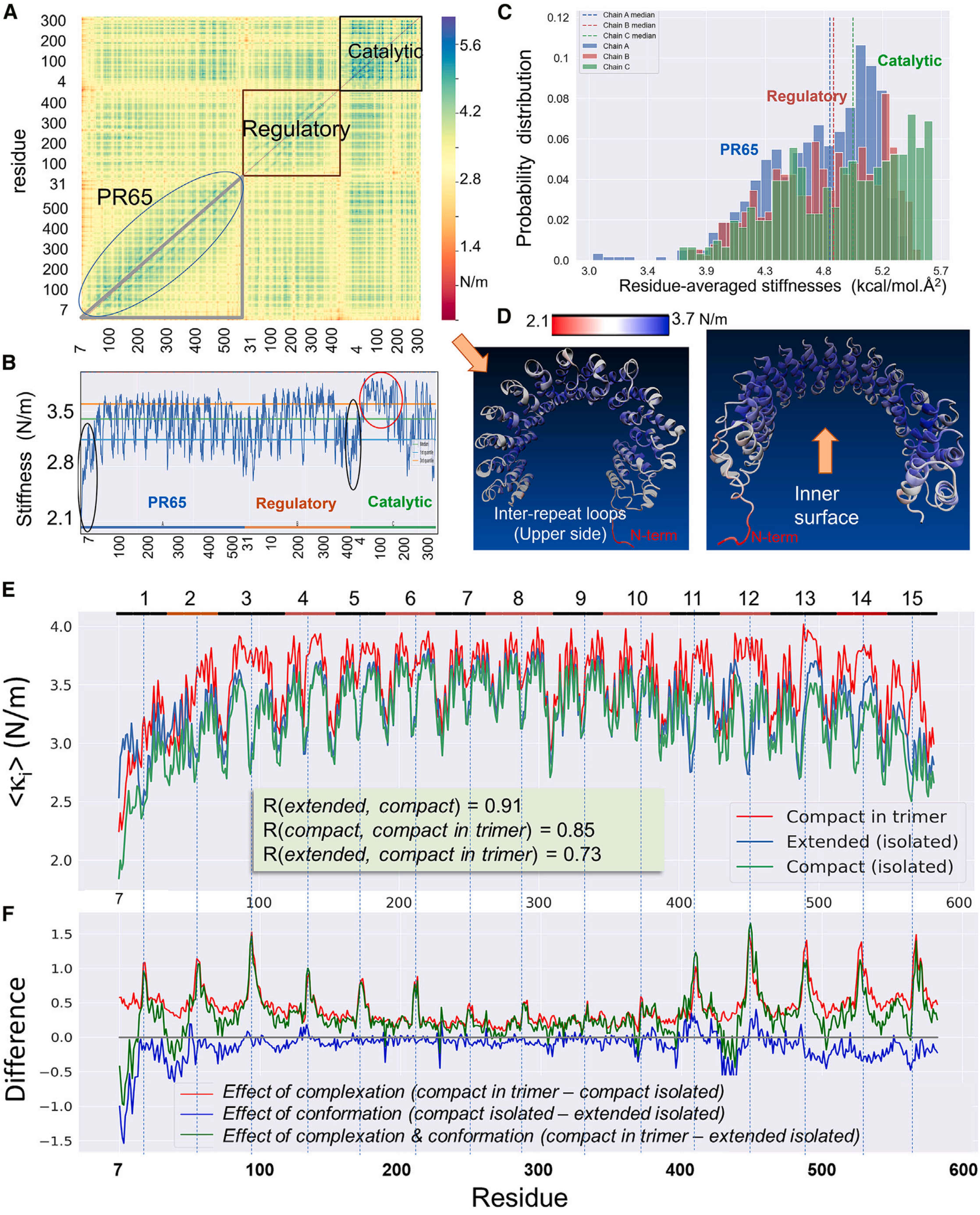

Figure 6. Mechanical properties of PR65

The resistance to uniaxial deformation is shown for PR65 in PP2A.

(A) Heatmap displaying the effective resistance $<\kappa_{ij}>$ of PP2A to deformation upon application of a uniaxial deformation to any pair of residues *i* and *j*. Residue numbers along the axes refer to those of the three subunits resolved in the examined structure (PDB: 2iae). Strongest resistance is observed at the catalytic domain.

(B) $<\kappa_i>$ for each residue *i*, averaged over all pairs (*i*, *j*). The N terminus is highly yielding (enclosed in black ellipse), while the *dom1* of the catalytic subunit (red ellipse) shows high resistance to deformation.

(C) Distribution of $<\kappa_i>$ in kcal/(mol.Å^2).

(D) Dependency of $<\kappa_i>$ on position *i*. See also Figure S6A.

(E) Mechanical resistance of PR65 to uniaxial deformation and its stiffening in PP2A. Results are presented for PR65 compact and extended forms (in isolation, respective green and blue curves) and PR65 (compact) in the trimer (red curve).

(F) Changes in stiffness between different forms, as indicated in the legend.

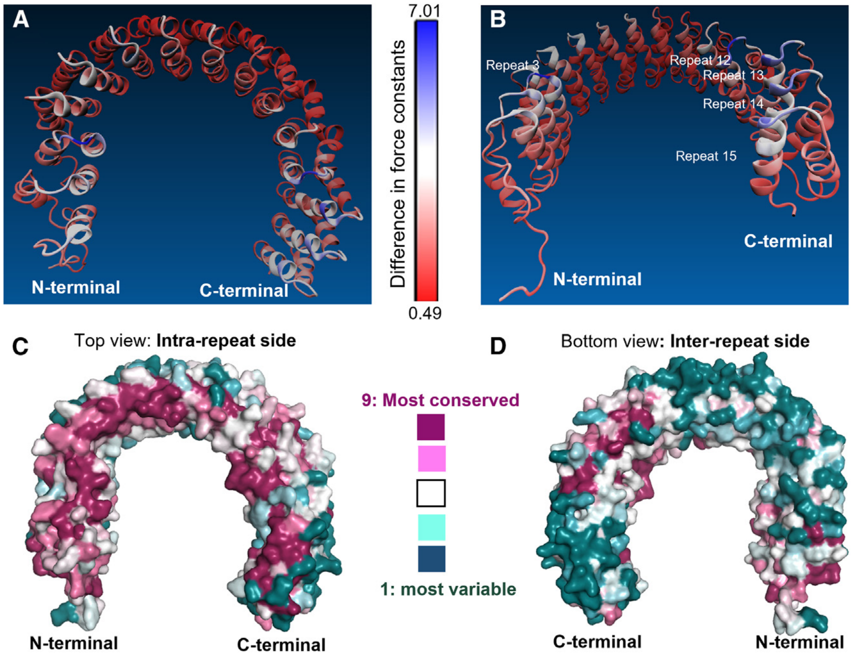

Figure 7. Evolutionary conservation of key mechanical regions of PR65

(A and B) The top (A) and bottom (B) views of the PR65 scaffold color coded by the changes in stiffness undergone in the compact form upon complexation (using the red curve in Figure 6F).

(C and D) The PR65 structure (in surface representation) from the top (C) and bottom (D), color-coded by the conservation of amino acids, as predicted by ConSurf (color code in the center).

of the catalytic subunit. Upon further complexation with the regulatory subunit, PR65 retains its softest modes of motion related to the expansion/contraction of the overall structure permitting distance changes of about 40 Å between its two ends. Trimerization induces, on the other hand, an enhanced cooperativity across the scaffold. Notably, in the trimeric PP2A, the catalytic subunit is sequestered between the C-terminal arm of PR65 and the C-terminal repeats of the regulatory subunit, both of which may concertedly assist in the catalytic interdomain cleft opening/closure for enzymatic activity.

The effective resistance $<\kappa_{ij}>$ of PR65 to uniaxial deformation lies in the range $2.0 \leq \kappa_{ij} \leq 4.5$ N/m (or 325 ± 125 pN/Å), depending on the pairs of residues (i, j) on which the stress is applied. Note that our previous study[29] for a series of proteins (tandem spectrin repeats,[40,41] enhanced yellow fluorescent protein,[42] fibronectin repeat domain 10, titin,[43] and protein L[44]) showed that the resistance $<\kappa_{1N}>$ to tension exerted at the ends ($i = 1$ and $j = N$) scaled linearly with unfolding force (in pulling experiments applied to N and C termini), with an increase in $<\kappa_{1N}>$ from 1.0 to 2.0 N/m accompanying an unfolding force increase from 30 to 160 pN, approximately. Furthermore, the response is anisotropic: it depends on the pairs of residues on which the forces are exerted. For example, GFP shows a variation from 116 to 548 pN.[45] Theoretically predicted $<\kappa_{ij}>$ values for five different pairs in GFP yielded a correlation of 0.94 with the unfolding forces measured by AFM.[29] Notably, the ANM force constant used therein was $\gamma = 0.25$ kcal/(mol Å^2), which is comparable with that determined for PR65 here upon comparing the ANM mode spectrum with full-atomic NMA spectrum.

In the previous work of Grinthal et al.,[11] 2-ns-long MD simulations were performed by applying a constant force at the two ends of the PR65, either in tension or compression mode. The scaffold behaved like an elastic medium under low force, whereas viscoelastic behavior prevailed under higher forces due to disruption of certain helix-helix interfaces. In contrast to these simulations, our aim was to observe the conformational behavior of PR65 scaffold in solution, closer to *in vivo* conditions. Our unbiased MD simulations as well as ClustENMD sampling pointed to the highly elastic character of this horseshoe-shaped scaffold with its highly variable end-to-end distance for the first time. These findings are consistent with the global modes of motions intrinsically accessible to the scaffold, as predicted by the ANM. Such global modes also underlie the allosteric dynamics of multimeric proteins.[36] In the present system, they mediate the cooperative action of the three subunits in PP2A. Global modes also facilitate the conformational transitions of the scaffold and the core enzyme during complexation. Specifically, the structural transitions undergone by the core enzyme (AC complex) during its binding to either the regulatory subunit or multiple subunits in the formation of the 12-meric INTAC are facilitated by the first two global modes.

The regions subject to mechanical constraints are also verified here to be evolutionarily conserved. In particular, the intra-repeat coil regions stiffen at the C-terminal arm of PR65 more than any other regions upon complexation with the regulatory and catalytic subunits, suggesting that they play a key role in establishing the allosteric communication across PR65. Not surprisingly, the intra-repeat coils are verified to be more conserved evolutionarily than the inter-repeat loops. Given their importance in establishing communication or substrate binding, as well as their adaptability (by virtue of their coiled structure), the intra-repeat regions appear to be strong candidates for amino acid substitutions or ligand binding toward redesigning PR65 or similar tandem-repeat proteins for customized functionalities. Of interest is a "vulnerable" region occupying a hinge-like site at the interface between repeats 11 and 12, which exhibited unusual changes (a softening) upon complexation in the trimeric PP2A. This region may be explored as a target site for modulating the dynamics, and thereby function, of PR65.

STAR★METHODS

Detailed methods are provided in the online version of this paper and include the following:

- KEY RESOURCES TABLE
- RESOURCE AVAILABILITY

- ○ Lead contact
  - ○ Materials availability
  - ○ Data and code availability
- ● METHOD DETAILS
  - ○ MD simulations
  - ○ Classical normal mode analysis (NMA)
  - ○ Anisotropic network model (ANM)
  - ○ Mechanical stiffness (Mechstiff)
  - ○ Hybrid simulations
- ● QUANTIFICATION AND STATISTICAL ANALYSIS

SUPPLEMENTAL INFORMATION

Supplemental information can be found online at https://doi.org/10.1016/j.str.2023.02.012.

ACKNOWLEDGMENTS

I.B., L.S.I., R.G., and S.-H.Y. gratefully acknowledge that this work was supported by a research grant from HFSP (reference no. RGP0027/2020). I.B. and P.D. also acknowledge partial support by NIH (R01 GM139297).

AUTHOR CONTRIBUTIONS

I.B., B.T.K., and P.D. conceptualized the study and designed it in coordination with L.S.I., R.G., and S.-H.Y. B.T.K., P.D., A.B., and Z.L.D. carried out the computations under the supervision of I.B. B.T.K., Z.L.D., P.D., A.B., and I.B. analyzed the data and prepared the tables and figures. S.-H.Y., R.G., L.S.I., and I.B. provided overall guidance and contributed to the interpretation of the results. I.B., P.D., Z.L.D., and B.T.K. contributed to the first draft of the manuscript, and all authors contributed to the final version. All authors have full access to data and accepted responsibility for the decision to submit for publication.

DECLARATION OF INTERESTS

The authors declare no competing interests.

INCLUSION AND DIVERSITY

We support inclusive, diverse, and equitable conduct of research.

Received: September 28, 2022
Revised: January 25, 2023
Accepted: February 23, 2023
Published: March 21, 2023

REFERENCES

1. Kajava, A.V. (2012). Tandem repeats in proteins: from sequence to structure. J. Struct. Biol. *179*, 279–288. https://doi.org/10.1016/j.jsb.2011.08.009.
2. Romera, D., Couleaud, P., Mejias, S.H., Aires, A., and Cortajarena, A.L. (2015). Biomolecular templating of functional hybrid nanostructures using repeat protein scaffolds. Biochem. Soc. Trans. *43*, 825–831. https://doi.org/10.1042/BST20150077.
3. Tsytlonok, M., Craig, P.O., Sivertsson, E., Serquera, D., Perrett, S., Best, R.B., Wolynes, P.G., and Itzhaki, L.S. (2013). Complex energy landscape of a giant repeat protein. Structure *21*, 1954–1965. https://doi.org/10.1016/j.str.2013.08.028.
4. Jost, C., and Plückthun, A. (2014). Engineered proteins with desired specificity: DARPins, other alternative scaffolds and bispecific IgGs. Curr. Opin. Struct. Biol. *27*, 102–112. https://doi.org/10.1016/j.sbi.2014.05.011.
5. Ferreiro, D.U., Walczak, A.M., Komives, E.A., and Wolynes, P.G. (2008). The energy landscapes of repeat-containing proteins: topology, cooperativity, and the folding funnels of one-dimensional architectures. PLoS Comput. Biol. *4*, e1000070. https://doi.org/10.1371/journal.pcbi.1000070.
6. Barrick, D., Ferreiro, D.U., and Komives, E.A. (2008). Folding landscapes of ankyrin repeat proteins: experiments meet theory. Curr. Opin. Struct. Biol. *18*, 27–34. https://doi.org/10.1016/j.sbi.2007.12.004.
7. Synakewicz, M., Eapen, R.S., Perez-Riba, A., Rowling, P.J.E., Bauer, D., Weißl, A., Fischer, G., Hyvönen, M., Rief, M., Itzhaki, L.S., and Stigler, J. (2022). Unraveling the mechanics of a repeat-protein nanospring: from folding of individual repeats to fluctuations of the superhelix. ACS Nano *16*, 3895–3905. https://doi.org/10.1021/acsnano.1c09162.
8. Baclayon, M., Ulsen, P.v., Mouhib, H., Shabestari, M.H., Verzijden, T., Abeln, S., Roos, W.H., and Wuite, G.J.L. (2016). Mechanical unfolding of an autotransporter passenger protein reveals the secretion starting point and processive transport intermediates. ACS Nano *10*, 5710–5719. https://doi.org/10.1021/acsnano.5b07072.
9. Cohen, S.S., Riven, I., Cortajarena, A.L., De Rosa, L., D'Andrea, L.D., Regan, L., and Haran, G. (2015). Probing the molecular origin of native-state flexibility in repeat proteins. J. Am. Chem. Soc. *137*, 10367–10373. https://doi.org/10.1021/jacs.5b06160.
10. Lamboy, J.A., Kim, H., Lee, K.S., Ha, T., and Komives, E.A. (2011). Visualization of the nanospring dynamics of the IkappaBalpha ankyrin repeat domain in real time. Proc. Natl. Acad. Sci. USA *108*, 10178–10183. https://doi.org/10.1073/pnas.1102226108.
11. Grinthal, A., Adamovic, I., Weiner, B., Karplus, M., and Kleckner, N. (2010). PR65, the HEAT-repeat scaffold of phosphatase PP2A, is an elastic connector that links force and catalysis. Proc. Natl. Acad. Sci. USA *107*, 2467–2472. https://doi.org/10.1073/pnas.0914073107.
12. Serquera, D., Lee, W., Settanni, G., Marszalek, P.E., Paci, E., and Itzhaki, L.S. (2010). Mechanical unfolding of an ankyrin repeat protein. Biophys. J. *98*, 1294–1301. https://doi.org/10.1016/j.bpj.2009.12.4287.
13. Kappel, C., Zachariae, U., Dölker, N., and Grubmüller, H. (2010). An unusual hydrophobic core confers extreme flexibility to HEAT repeat proteins. Biophys. J. *99*, 1596–1603. https://doi.org/10.1016/j.bpj.2010.06.032.
14. Kim, M., Abdi, K., Lee, G., Rabbi, M., Lee, W., Yang, M., Schofield, C.J., Bennett, V., and Marszalek, P.E. (2010). Fast and forceful refolding of stretched alpha-helical solenoid proteins. Biophys. J. *98*, 3086–3092. https://doi.org/10.1016/j.bpj.2010.02.054.
15. Zachariae, U., and Grubmüller, H. (2008). Importin-beta: structural and dynamic determinants of a molecular spring. Structure *16*, 906–915. https://doi.org/10.1016/j.str.2008.03.007.
16. Forwood, J.K., Lange, A., Zachariae, U., Marfori, M., Preast, C., Grubmüller, H., Stewart, M., Corbett, A.H., and Kobe, B. (2010). Quantitative structural analysis of importin-beta flexibility: paradigm for solenoid protein structures. Structure *18*, 1171–1183. https://doi.org/10.1016/j.str.2010.06.015.
17. Sotomayor, M., Corey, D.P., and Schulten, K. (2005). In search of the hair-cell gating spring elastic properties of ankyrin and cadherin repeats. Structure *13*, 669–682. https://doi.org/10.1016/j.str.2005.03.001.
18. Fukuhara, N., Fernandez, E., Ebert, J., Conti, E., and Svergun, D. (2004). Conformational variability of nucleo-cytoplasmic transport factors. J. Biol. Chem. *279*, 2176–2181. https://doi.org/10.1074/jbc.M309112200.
19. Courtemanche, N., and Barrick, D. (2008). The leucine-rich repeat domain of Internalin B folds along a polarized N-terminal pathway. Structure *16*, 705–714. https://doi.org/10.1016/j.str.2008.02.015.
20. Kloss, E., Courtemanche, N., and Barrick, D. (2008). Repeat-protein folding: new insights into origins of cooperativity, stability, and topology. Arch. Biochem. Biophys. *469*, 83–99. https://doi.org/10.1016/j.abb.2007.08.034.
21. Werbeck, N.D., and Itzhaki, L.S. (2007). Probing a moving target with a plastic unfolding intermediate of an ankyrin-repeat protein. Proc. Natl. Acad. Sci. USA *104*, 7863–7868. https://doi.org/10.1073/pnas.0610315104.
22. Cho, U.S., and Xu, W. (2007). Crystal structure of a protein phosphatase 2A heterotrimeric holoenzyme. Nature *445*, 53–57. https://doi.org/10.1038/nature05351.
23. Sangodkar, J., Farrington, C.C., McClinch, K., Galsky, M.D., Kastrinsky, D.B., and Narla, G. (2016). All roads lead to PP2A: exploiting the

therapeutic potential of this phosphatase. FEBS J. *283*, 1004–1024. https://doi.org/10.1111/febs.13573.

24. O'Connor, C.M., Perl, A., Leonard, D., Sangodkar, J., and Narla, G. (2018). Therapeutic targeting of PP2A. Int. J. Biochem. Cell Biol. *96*, 182–193. https://doi.org/10.1016/j.biocel.2017.10.008.
25. Groves, M.R., Hanlon, N., Turowski, P., Hemmings, B.A., and Barford, D. (1999). The structure of the protein phosphatase 2A PR65/A subunit reveals the conformation of its 15 tandemly repeated HEAT motifs. Cell *96*, 99–110. https://doi.org/10.1016/s0092-8674(00)80963-0.
26. Atilgan, A.R., Durell, S.R., Jernigan, R.L., Demirel, M.C., Keskin, O., and Bahar, I. (2001). Anisotropy of fluctuation dynamics of proteins with an elastic network model. Biophys. J. *80*, 505–515. https://doi.org/10.1016/S0006-3495(01)76033-X.
27. Kurkcuoglu, Z., Bahar, I., and Doruker, P. (2016). ClustENM: ENM-based sampling of essential conformational space at full atomic resolution. J. Chem. Theory Comput. *12*, 4549–4562. https://doi.org/10.1021/acs.jctc.6b00319.
28. Kaynak, B.T., Zhang, S., Bahar, I., and Doruker, P. (2021). ClustENMD: efficient sampling of biomolecular conformational space at atomic resolution. Bioinformatics *37*, 3956–3958. https://doi.org/10.1093/bioinformatics/btab496.
29. Eyal, E., and Bahar, I. (2008). Toward a molecular understanding of the anisotropic response of proteins to external forces: insights from elastic network models. Biophys. J. *94*, 3424–3435. https://doi.org/10.1529/biophysj.107.120733.
30. Eyal, E., Dutta, A., and Bahar, I. (2011). Cooperative dynamics of proteins unraveled by network models. Wiley Interdiscip. Rev. Comput. Mol. Sci. *1*, 426–439. https://doi.org/10.1002/wcms.44.
31. Bahar, I., Lezon, T.R., Yang, L.W., and Eyal, E. (2010). Global dynamics of proteins: bridging between structure and function. Annu. Rev. Biophys. *39*, 23–42. https://doi.org/10.1146/annurev.biophys.093008.131258.
32. Kaynak, B.T., Krieger, J.M., Dudas, B., Dahmani, Z.L., Costa, M.G.S., Balog, E., Scott, A.L., Doruker, P., Perahia, D., and Bahar, I. (2022). Sampling of protein conformational space using hybrid simulations: a critical assessment of recent methods. Front. Mol. Biosci. *9*, 832847. https://doi.org/10.3389/fmolb.2022.832847.
33. Xing, Y., Xu, Y., Chen, Y., Jeffrey, P.D., Chao, Y., Lin, Z., Li, Z., Strack, S., Stock, J.B., and Shi, Y. (2006). Structure of protein phosphatase 2A core enzyme bound to tumor-inducing toxins. Cell *127*, 341–353. https://doi.org/10.1016/j.cell.2006.09.025.
34. Zheng, H., Qi, Y., Hu, S., Cao, X., Xu, C., Yin, Z., Chen, X., Li, Y., Liu, W., Li, J., et al. (2020). Identification of Integrator-PP2A complex (INTAC), an RNA polymerase II phosphatase. Science *370*, eabb5872. https://doi.org/10.1126/science.abb5872.
35. Zhang, S., Krieger, J.M., Zhang, Y., Kaya, C., Kaynak, B., Mikulska-Ruminska, K., Doruker, P., Li, H., and Bahar, I. (2021). ProDy 2.0: increased scale and scope after 10 Years of protein dynamics modelling with Python. Bioinformatics *37*, 3657–3659. https://doi.org/10.1093/bioinformatics/btab187.
36. Zhang, Y., Doruker, P., Kaynak, B., Zhang, S., Krieger, J., Li, H., and Bahar, I. (2020). Intrinsic dynamics is evolutionarily optimized to enable allosteric behavior. Curr. Opin. Struct. Biol. *62*, 14–21. https://doi.org/10.1016/j.sbi.2019.11.002.
37. Liu, Y., and Bahar, I. (2012). Sequence evolution correlates with structural dynamics. Mol. Biol. Evol. *29*, 2253–2263. https://doi.org/10.1093/molbev/mss097.
38. Landau, M., Mayrose, I., Rosenberg, Y., Glaser, F., Martz, E., Pupko, T., and Ben-Tal, N. (2005). ConSurf 2005: the projection of evolutionary conservation scores of residues on protein structures. Nucleic Acids Res. *33*, W299–W302. https://doi.org/10.1093/nar/gki370.
39. Ashkenazy, H., Abadi, S., Martz, E., Chay, O., Mayrose, I., Pupko, T., and Ben-Tal, N. (2016). ConSurf 2016: an improved methodology to estimate and visualize evolutionary conservation in macromolecules. Nucleic Acids Res. *44*, W344–W350. https://doi.org/10.1093/nar/gkw408.
40. Law, R., Carl, P., Harper, S., Dalhaimer, P., Speicher, D.W., and Discher, D.E. (2003). Cooperativity in forced unfolding of tandem spectrin repeats. Biophys. J. *84*, 533–544. https://doi.org/10.1016/S0006-3495(03)74872-3.
41. Rief, M., Pascual, J., Saraste, M., and Gaub, H.E. (1999). Single molecule force spectroscopy of spectrin repeats: low unfolding forces in helix bundles. J. Mol. Biol. *286*, 553–561. https://doi.org/10.1006/jmbi.1998.2466.
42. Perez-Jimenez, R., Garcia-Manyes, S., Ainavarapu, S.R.K., and Fernandez, J.M. (2006). Mechanical unfolding pathways of the enhanced yellow fluorescent protein revealed by single molecule force spectroscopy. J. Biol. Chem. *281*, 40010–40014. https://doi.org/10.1074/jbc.M609890200.
43. Li, H., and Fernandez, J.M. (2003). Mechanical design of the first proximal Ig domain of human cardiac titin revealed by single molecule force spectroscopy. J. Mol. Biol. *334*, 75–86. https://doi.org/10.1016/j.jmb.2003.09.036.
44. Brockwell, D.J., Beddard, G.S., Paci, E., West, D.K., Olmsted, P.D., Smith, D.A., and Radford, S.E. (2005). Mechanically unfolding the small, topologically simple protein L. Biophys. J. *89*, 506–519. https://doi.org/10.1529/biophysj.105.061465.
45. Dietz, H., Berkemeier, F., Bertz, M., and Rief, M. (2006). Anisotropic deformation response of single protein molecules. Proc. Natl. Acad. Sci. USA *103*, 12724–12728. https://doi.org/10.1073/pnas.0602995103.
46. Phillips, J.C., Hardy, D.J., Maia, J.D.C., Stone, J.E., Ribeiro, J.V., Bernardi, R.C., Buch, R., Fiorin, G., Hénin, J., Jiang, W., et al. (2020). Scalable molecular dynamics on CPU and GPU architectures with NAMD. J. Chem. Phys. *153*, 044130. https://doi.org/10.1063/5.0014475.
47. Brooks, B.R., Brooks, C.L., 3rd, Mackerell, A.D., Jr., Nilsson, L., Petrella, R.J., Roux, B., Won, Y., Archontis, G., Bartels, C., Boresch, S., et al. (2009). CHARMM: the biomolecular simulation program. J. Comput. Chem. *30*, 1545–1614. https://doi.org/10.1002/jcc.21287.
48. Bakan, A., Meireles, L.M., and Bahar, I. (2011). ProDy: protein dynamics inferred from theory and experiments. Bioinformatics *27*, 1575–1577. https://doi.org/10.1093/bioinformatics/btr168.
49. Huang, J., and MacKerell, A.D., Jr. (2013). CHARMM36 all-atom additive protein force field: validation based on comparison to NMR data. J. Comput. Chem. *34*, 2135–2145. https://doi.org/10.1002/jcc.23354.
50. Huang, J., Rauscher, S., Nawrocki, G., Ran, T., Feig, M., de Groot, B.L., Grubmüller, H., and MacKerell, A.D., Jr. (2017). CHARMM36m: an improved force field for folded and intrinsically disordered proteins. Nat. Methods *14*, 71–73. https://doi.org/10.1038/nmeth.4067.
51. Jo, S., Kim, T., Iyer, V.G., and Im, W. (2008). CHARMM-GUI: a web-based graphical user interface for CHARMM. J. Comput. Chem. *29*, 1859–1865. https://doi.org/10.1002/jcc.20945.
52. Eyal, E., Lum, G., and Bahar, I. (2015). The anisotropic network model web server at 2015 (ANM 2.0). Bioinformatics *31*, 1487–1489. https://doi.org/10.1093/bioinformatics/btu847.
53. Eyal, E., Chennubhotla, C., Yang, L.W., and Bahar, I. (2007). Anisotropic fluctuations of amino acids in protein structures: insights from X-ray crystallography and elastic network models. Bioinformatics *23*, i175–i184. https://doi.org/10.1093/bioinformatics/btm186.
54. Hinsen, K. (2008). Structural flexibility in proteins: impact of the crystal environment. Bioinformatics *24*, 521–528. https://doi.org/10.1093/bioinformatics/btm625.
55. Na, H., Hinsen, K., and Song, G. (2021). The amounts of thermal vibrations and static disorder in protein X-ray crystallographic B-factors. Proteins *89*, 1442–1457. https://doi.org/10.1002/prot.26165.
56. Mikulska-Ruminska, K., Kulik, A.J., Benadiba, C., Bahar, I., Dietler, G., and Nowak, W. (2017). Nanomechanics of multidomain neuronal cell adhesion protein contactin revealed by single molecule AFM and SMD. Sci. Rep. *7*, 8852. https://doi.org/10.1038/s41598-017-09482-w.

STAR★METHODS

KEY RESOURCES TABLE

REAGENT or RESOURCE	SOURCE	IDENTIFIER
Deposited data		
Apo structure of PR65	Groves et al.[25]	PDB: 1B3U
Structure of hetero-trimeric complex PP2A	Cho et al.[22]	PDB: 2IAE
Structure of the Protein Phosphatase 2A Core Enzyme	Xing et al.[33]	PDB: 2IE3
Structure of Integrator-PP2A complex (INTAC)	Zheng et al.[34]	PDB: 7CUN
Software and algorithms		
NAMD 2.13	Phillips et al.[46]	http://www.ks.uiuc.edu/Research/namd/
VIBRAN module of CHARMM-GUI	Brooks et al.[47]	https://www.charmm-gui.org/charmmdoc/vibran.html
ANM module in ProDy 2.0	Zhang et al., Bakan et al.[35,48]	http://prody.csb.pitt.edu/
MechStiff module in ProDy 2.0	Zhang et al., Bakan et al.[35,48]	http://prody.csb.pitt.edu/
ClustENMD	Kaynak et al.[28]	http://prody.csb.pitt.edu/clustenmd/
ConSurf	Landau et al., Ashkenazy et al.[38,39]	https://consurf.tau.ac.il/consurf_index.php

RESOURCE AVAILABILITY

Lead contact

All requests should be directed to and will be fulfilled by the Lead Contact, Ivet Bahar (bahar@laufercenter.org).

Materials availability

This study did not generate new unique reagents.

Data and code availability

- This paper analyzes existing, publicly available data. These accession numbers for the datasets are listed in the key resources table.
- All data reported in this paper will be shared by the lead contact upon request.
- The source code for all computations and input/output data are available upon request. ANM, Mechanical Stiffness, ClustENMD analysis have been conducted using *ProDy*, an open-source API freely available on the web via http://prody.csb.pitt.edu/. MD analysis have been performed using NAMD and NMA analysis have been performed using VIBRAN module of CHARMM.
- MD trajectories will be provided on request.
- Any additional information required to reanalyze the data reported in this paper is available from the lead contact upon request (bahar@laufercenter.org).

METHOD DETAILS

MD simulations

Four independent runs, each of 200 ns duration, were performed using NAMD[46] for PR65 scaffold in explicit solvent. NPT simulations were carried out at 303.15 K and 1 atm (2 fs time step) using the additive c36m force field.[49,50] Two of the runs (named as *E1* and *E2*) were initiated from the apo structure of PR65 (PDB id: 1b3u), which is in an *extended* conformation. The remaining two runs (*C1* and *C2*) were based on a more *compact* conformer of PR65, which is extracted from the hetero-trimeric complex PP2A (PDB id: 2iae). Extended and compact structures correspond to *magenta* and *cyan* conformers aligned in Figure 1B. The initial systems were prepared in explicit solvent using the default procedure of system preparation on CHARMM-GUI server.[51]

Classical normal mode analysis (NMA)

All-atom normal modes were calculated using the VIBRAN module of CHARMM software.[47] To compare the vibrational frequencies of PR65 extended and compact states, a representative conformer was chosen from the initial stage (between 1 and 5 ns) of each independent MD run, leading to four conformers in total (*E1, E2, C1, C2*). Prior to NMA, extensive energy minimization was performed on each conformer in vacuum after extracting the protein from the periodic box. The potential energy was minimized until an energy RMS gradient of 10^{-5} kcal/mol/Å was reached. Then, normal modes were calculated using the VIBRAN module with the additive c36m force field.[49,50]

Anisotropic network model (ANM)

To observe the effect of conformational flexibility on global dynamics, we used the widely used elastic network model ANM.[26,52] ANM analysis implemented in *ProDy* API[35,48] was adopted with the default cutoff radius of 15 Å between α-carbons. Calculations were repeated for a series of MD snapshots to allow for a broader distribution of accessible motions. In the ANM analysis, the Hessian matrix of the second derivatives of the overall potential with respect to displacements is a $3N \times 3N$ matrix (for a structure of N residues), is constructed based on harmonic potentials with uniform force constant γ between all residue pairs connected by a spring (i.e., within the cutoff-distance).[26,30,31,52] The Hessian can thus be written as γH after factoring out the uniform force constant. As in classical NMA, the frequencies and shapes of collective modes are determined by eigenvalue decomposition of H. The absolute value of γ does not affect the relative frequencies (obtained from the eigenvalues of H) nor the relative distribution of residue motions (represented by the eigenvectors of H), but uniformly rescales their size.[26,29] The cross-correlation $<\Delta R_i \cdot \Delta R_j>_{ANM}$ between the fluctuations ΔR_i and ΔR_j of residues *i* and *j* is given by

$$\langle \Delta R_i \cdot \Delta R_j \rangle_{ANM} = (k_B T / \gamma) tr\left[H^{-1}\right]_{ij} = (k_B T / \gamma) \sum_{k=1}^{3N-6} (1/\lambda_k) tr\left[\boldsymbol{u}_i^{(k)} \boldsymbol{u}_j^{(k)T}\right]_{ij} \qquad \text{(Equation 1)}$$

where $tr[\mathbf{H}^{-1}]_{ij}$ is the trace of the ij^{th} 3 × 3 submatrix of the pseudoinverse of **H**, λ_k and $\boldsymbol{u}^{(k)}$ are the k^{th} eigenvalue and eigenvector of **H**, $\boldsymbol{u}_i^{(k)}$ is the i^{th} super-element (a 3D vector) of $\boldsymbol{u}^{(k)}$ describing the i^{th} residue/node motion in 3D along mode *k*, k_B is the Boltzmann constant, T is the absolute temperature, and the summation is carried out over all *3N-6* modes. The mean-square fluctuations (MSFs) of residues, $<(\Delta R_i)^2>_{ANM}$, are given by the same equation, with $i = j$. A common practice has been to evaluate γ upon comparison of the $<(\Delta R_i)^2>_{ANM}$ profile with that inferred from X-ray crystallographic B-factors[53] using

$$B_i = 8\pi^2 / 3\langle (R_i)^2 \rangle_{exp} \qquad \text{(Equation 2)}$$

which upon comparison with Equation 1 yields the average force constant adopted in the ANM

$$\gamma = \left(\frac{k_B \mathrm{T}}{N}\right) \sum_{i=1}^{N} (8\pi^2 / 3)\ tr\left[H^{-1}\right]_{ii} / B_i \qquad \text{(Equation 3)}$$

Here B_i is the B-factor reported in the PDB for the i^{th} α-carbon. However, the use of B factors for calibration has limitations,[54,55] as they refer to crystallographic conditions, i.e., they depend on the crystallization conditions as well as intermolecular contacts that are artifacts of the crystal lattice environment. Instead, we adopt here an alternative route for evaluating γ. ANM-predicted eigenvalues (λ_k) are related to the mode frequencies ω_k obtained by classical full-atomic NMA as

$$\omega_k = (1/2\pi)(\gamma \lambda_k / m)^{1/2} \qquad \text{(Equation 4)}$$

where *m* is the mass of ANM nodes, each representing a residue. Here we use the average ($<m> = 150.7$ g/mol) over all twenty types of amino acids. The above relationship permits us to evaluate the force constant γ consistent with the frequencies of the global modes computed by full-atomic NMA, using for example the slope of the plot of ω_k against $\lambda_k{}^{1/2}$, and use γ for calculating material properties such as resistance to deformation, as explained next. As to the mode shapes predicted by ANM and NMA, we simply evaluate the correlation cosine, also called *overlap*, between the two sets of eigenvectors, as the eigenvectors are, by definition, normalized.

Mechanical stiffness (Mechstiff)

The mechanical stiffness, or the *resistance to deformation* in response to uniaxial tension was computed using the *Mechstiff* module of *ProDy* implemented[56] after the theory introduced by Eyal and Bahar.[29,30] The approach allows for generating an $N \times N$ heatmap for the effective stiffness (or effective resistance or force constant, $< \kappa_{ij} >$) for each residue pair in response to uniaxial tension applied at those particular pair (*i, j*) for a protein of *N* residues, using

$$\langle \boldsymbol{\kappa}_{\mathbf{ij}} \rangle = \sum_{(\mathbf{k})} d_{ij}^{(k)} \gamma \lambda_k \Bigg/ \sum_{(\mathbf{k})} d_{ij}^{(k)} \qquad \text{(Equation 5)}$$

where $d_{ij}^{(k)}$ is the contribution of the k^{th} mode to the deformation imposed by the exerted force, given by

$$d_{ij}^{(k)} = \left(k_{BT/}\gamma \lambda_k\right)^{\frac{1}{2}}\ cos\ \alpha_{ij}{}^{(k)} \left| \boldsymbol{u}_i^{(k)} - \boldsymbol{u}_j^{(k)} \right| \qquad \text{(Equation 6)}$$

Here $\alpha_{ij}{}^{(k)}$ is the angle between the direction of the external force and that of the change $\Delta \boldsymbol{R}_{ij}^{(k)}$ in inter-residue distance induced by mode *k*. As may be seen from Equation 5, the value of effective stiffness is lower if the deformation is accommodated by soft modes and vice versa.

Hybrid simulations

We used ClustENMD[28] for sampling the ensemble of conformers accessible to (a) the heterotrimeric PP2A, (b) the dimer formed by the PR65 and catalytic subunits, and (c) PR65, all using structural data from the crystal structure of PP2A (PDB id: 2iae). ClustENMD is a hybrid technique that allows for sampling the conformational space of the examined biomolecular system, guided by ANM, and complemented by clustering of conformers to identify representatives using MD simulations at 303.15 K in implicit solvent. It is particularly suitable for exploring the conformational space of multimeric proteins, as shown in a recent comparative study.[32] We performed two independent ClustENMD runs for each of the three systems a-c and generated 600 conformers for each system. Each run was composed of 5 generations of conformational sampling with 1 Å average deformation each, using random combinations of the three lowest frequency ANM modes. Short MD simulations were performed for relaxation of each representative conformer.

QUANTIFICATION AND STATISTICAL ANALYSIS

We carried out four independent MD simulation runs, each of 200 ns duration, using NAMD for the PR65 scaffold in explicit solvent. The fluctuations in PR65 inter-repeat distances, $d_{1\text{-}15}$ and $d_{5\text{-}11,}$ during these MD simulations are provided in Figure 2. We further carried out ANM analysis on all MD snapshots and reported distributions of global mode frequencies (Figure 2). We carried out normal mode analysis on four representative conformations chosen between 1 and 5 ns of each independent MD run to report global mode frequencies. We performed two independent ClustENMD runs for each of the following systems- (a) the heterotrimeric PP2A, (b) the dimer formed by the PR65 and catalytic subunits, and (c) PR65, all using structural data from the crystal structure of PP2A, and generated 600 conformers for further analysis of dynamics features (Figures 3 and 4). The *Mechstiff* module of ProDy was used to compute the mechanical stiffness for different crystal structures of PR65 and PP2A (Figure 6).